Arbitrary Lagrangian–Eulerian (ALE) formulation for hyperelastoplasticity

Antonio Rodríguez-Ferran*,†, Agustí Pérez-Foguet and Antonio Huerta

Departament de Matemàtica Aplicada III, E.T.S. de Ingenieros de Caminos, Canales y Puertos, Universitat Politècnica de Catalunya, Jordi Girona 1, E-08034 Barcelona, Spain

SUMMARY

The arbitrary Lagrangian–Eulerian (ALE) description in non-linear solid mechanics is nowadays standard for hypoelastic–plastic models. An extension to hyperelastic–plastic models is presented here. A fractional-step method—a common choice in ALE analysis—is employed for time-marching: every time-step is split into a Lagrangian phase, which accounts for material effects, and a convection phase, where the relative motion between the material and the finite element mesh is considered. In contrast to previous ALE formulations of hyperelasticity or hyperelastoplasticity, the deformed configuration at the beginning of the time-step, not the initial undeformed configuration, is chosen as the reference configuration. As a consequence, convecting variables are required in the description of the elastic response. This is not the case in previous formulations, where only the plastic response contains convection terms. In exchange for the extra convective terms, however, the proposed ALE approach has a major advantage: only the quality of the mesh in the spatial domain must be ensured by the ALE remeshing strategy; in previous formulations, it is also necessary to keep the distortion of the mesh in the material domain under control. Thus, the full potential of the ALE description as an adaptive technique can be exploited here. These aspects are illustrated in detail by means of three numerical examples: a necking test, a coining test and a powder compaction test.

KEY WORDS: arbitrary Lagrangian–Eulerian formulation; hyperelastoplasticity; finite strains; non-linear solid mechanics

1. INTRODUCTION

The arbitrary Lagrangian–Eulerian (ALE) formulation is a standard approach in large strain solid mechanics to keep mesh distortion and element entanglement" under control [1–6]. The basic idea of the ALE formulation is the use of a referential domain for the description of motion, different from the material domain (Lagrangian description) and the spatial domain

―――――――――
*Correspondence to: Antonio Rodríguez-Ferran, Departament de Matemàtica Aplicada III, E.T.S. de Ingenieros de Caminos, Canales y Puertos, Universitat Politècnica de Catalunya, Jordi Girona 1, E-08034 Barcelona, Spain
†E-mail: antonio.rodriguez-ferran@upc.es

(Eulerian description). When compared to fluid dynamics, where the ALE formulation originated (see Reference [7] and references therein), the main difficulty of ALE solid mechanics is the path-dependent behaviour of plasticity models. The relative motion between the mesh and the material must be accounted for in the treatment of the constitutive equation.

Two approaches may be used to describe large (elastic and inelastic) strains. In hypoelastic–plastic models [8–10], the evolution of stresses is expressed in rate format, relating an objective stress rate with a rate of deformation. In hyperelastic–plastic models [8–11], on the contrary, there is no rate equation for stresses: they can be computed from the deformation gradient via direct functional evaluation of the free energy function. However, the plastic response is still described in rate form, involving the Lie derivative.

Various formulations for large strain solid mechanics which combine an ALE kinematic description and hypoelastic–plastic models can be found in the literature [1–6]. In all of them, a key issue is the ALE convective term in the rate equation for stresses, which reflects the relative motion between the mesh and the material. The most popular approach to deal with this convective term is the use of a split or fractional-step method. Each time-step is divided into a material phase and a convection phase. Convection is neglected in the material phase, which is thus identical to a time-step in a standard Lagrangian analysis. After that, stresses and plastic internal variables are transported to account for the relative mesh-material motion in the convection phase.

On the other hand, ALE formulations for hyperelastoplasticity are not standard. In the context of incompressible hyperelasticity (i.e., no plastic strains), Reference [12] proposes an ALE finite element method with no need of convecting variables. The basic idea is that the referential, material and spatial domains are linked by appropriate mappings, so the deformation gradient that relates the spatial and material domains (and hence the stresses) can be computed from the referential domain simply by applying the chain rule. However, as discussed later, the price to pay for this coupled, convection-free approach is high: the distortion must be controlled for the *two* mappings (referential to material and referential to spatial), rather than only one. If large plastic strains are also considered, convection of the internal plastic variables is needed, because a convective term appears in the rate equations describing the plastic response [13].

To summarize: using the total deformation gradient (from the current deformed configuration to the initial undeformed configuration) to describe the hyperelastic response [12, 13] leads to an algorithm with two major characteristics: (1) it forces ALE remeshing to prevent distortion in two mappings, instead of only one and (2) convection of plastic variables is still needed for the plastic response.

For this reason, a different ALE formulation for hyperelastoplasticity is proposed here. It is very similar to the split ALE formulations for hypoelastoplasticity discussed above. The hyperelastic part of the response is described, as in standard hyperelastic–plastic algorithms, by means of the incremental deformation gradient (relating the deformed configurations before and after the time-step) rather than the total deformation gradient. In fact, the last converged deformed configuration, rather than the initial undeformed configuration, is used as a reference. As a consequence, elastic strains must be transported during the convection step. In exchange for this, ALE remeshing must prevent distortion in only one mapping (from the referential to the spatial domains). Thus, the full potential of the ALE formulation as an *r*-adaptive technique (that is, an adaptive technique based on *r*elocating the nodes of a given mesh without changing its topology [14]) can be exploited.

The general case of non-isochoric plasticity is considered in this paper. This means that the volume change (i.e., the determinant of the deformation gradient) cannot be computed solely from the elastic strains, so it must also be convected. Thus, the following information must be transported: elastic strains, plastic internal variables and volume change.

An outline of paper follows. Finite-strain multiplicative plasticity in a standard Lagrangian setting is briefly reviewed in Section 2; first, the basic equations are summarized in Section 2.1 and then the implementation aspects are treated in Section 2.2. Basic ALE kinematics are covered in Section 3. The proposed ALE formulation for hyperelastoplasticity is presented in Section 4, and illustrated by means of some representative numerical examples in Section 5. Finally, Section 6 closes the paper with some concluding remarks.

2. $F^e F^p$ FINITE-STRAIN PLASTICITY IN A LAGRANGIAN SETTING

2.1. Basic equations

This section contains a very brief review of multiplicative finite-strain plasticity with a Lagrangian description. Only the basic ingredients which are later needed in Section 4 are discussed. Detailed presentations of $F^e F^p$ plasticity can be found in the textbooks [8, 11, 10].

Let $R_X \subset \mathbb{R}^{n_{\dim}}$ ($n_{\dim} = 2, 3$) be the material configuration of a continuum body with particles labelled by their initial position vector $X \in R_X$. The motion of the body is described by the one-parameter family of mappings $\varphi_t : R_X \mapsto \mathbb{R}^{n_{\dim}}$ with $t \in [0, T]$. $R_x = \varphi_t(R_X)$ is the spatial configuration of the body at time t, and $x = \varphi_t(X) = \varphi(X, t) \in R_x$ is the current position of the material particle X. In a Lagrangian setting, X are used as the independent variables in the description of motion. The fundamental unknown is the field of particle displacements u:

$$u(X, t) = x(X, t) - X \tag{1}$$

The deformation gradient is defined as

$$F(X, t) = \frac{\partial \varphi}{\partial X}(X, t) \tag{2}$$

and it is locally decomposed into elastic and plastic parts as

$$F = F^e F^p \tag{3}$$

Uncoupled isotropic hyperelastic behaviour is assumed, with the local thermodynamic state defined by means of the elastic left Cauchy–Green tensor

$$b^e = F^e F^{eT} \tag{4}$$

and a set of strain-like scalar internal variables $\alpha \in \mathbb{R}^{n_z}$. In this situation, the Kirchhoff stress tensor, τ, and the stress-like internal variables, q, conjugate to α, are given by

$$\tau = 2 \frac{dW^e}{db^e} b^e \quad \text{and} \quad q = -\frac{dW^p}{d\alpha} \tag{5}$$

where W^e and W^p are the elastic and plastic parts of the free energy function

$$W(b^e, \alpha) = W^e(b^e) + W^p(\alpha) \tag{6}$$

The Cauchy stress tensor $\boldsymbol{\sigma}$ is given by

$$\boldsymbol{\sigma} = \frac{\boldsymbol{\tau}}{\det(\boldsymbol{F})} \tag{7}$$

In Equation (7), $\det(\boldsymbol{F})$ accounts for the volume change. For isochoric plasticity (i.e., no plastic volume change), $\det(\boldsymbol{F}^{\mathrm{p}}) = 1$ together with Equations (3) and (4) result in $\det(\boldsymbol{F}) = \sqrt{\det(\boldsymbol{b}^{\mathrm{e}})}$. For the general case of non-isochoric plasticity considered here, on the contrary, this equation does not hold.

The material time derivative of $\det(\boldsymbol{F})$ is given by the general relationship

$$\left.\frac{\partial |\boldsymbol{F}|}{\partial t}\right|_X = |\boldsymbol{F}| \nabla_x \cdot \boldsymbol{v} \tag{8}$$

where, following standard notation, $|_X$ means "holding the material particle X fixed", $\nabla_x \cdot \boldsymbol{v}$ is the divergence of the particle velocity $\boldsymbol{v} = \partial \boldsymbol{x}/\partial t|_X$ and $|\cdot|$ denotes the determinant.

Remark 1. In a standard Lagrangian analysis, $\det(\boldsymbol{F})$ is typically *not* updated via direct numerical time-integration of Equation (8). This rate equation will be useful in Section 4 to discuss the treatment of volume change in an ALE setting.

The plastic response of the material is assumed isotropic and defined by a yield function f,

$$f(\boldsymbol{\tau}, \mathbf{q}) = 0 \tag{9}$$

and the generic flow rules

$$\mathcal{L}_v \boldsymbol{b}^{\mathrm{e}} := \dot{\boldsymbol{b}}^{\mathrm{e}} - \boldsymbol{l}\boldsymbol{b}^{\mathrm{e}} - \boldsymbol{b}^{\mathrm{e}}\boldsymbol{l}^{\mathrm{T}} = -2\dot{\gamma}\boldsymbol{m}_\tau(\boldsymbol{\tau}, \mathbf{q})\,\boldsymbol{b}^{\mathrm{e}} \tag{10}$$

$$\dot{\boldsymbol{\alpha}} = \dot{\gamma}\boldsymbol{m}_{\mathbf{q}}(\boldsymbol{\tau}, \mathbf{q}) \tag{11}$$

where $\mathcal{L}_v$ is the Lie derivative with respect to the particle velocity $\boldsymbol{v}$, which involves the velocity gradient $\boldsymbol{l}$, $\boldsymbol{m}_\tau$ and $\boldsymbol{m}_{\mathbf{q}}$ are the flow directions and $\dot{\gamma}$ is the plastic multiplier, determined with the classical Kuhn–Tucker conditions. The superposed dot denotes material time derivative (that is, holding fixed the material particle X).

Equation (10) can also be written in terms of the strain measure $\boldsymbol{G}^{\mathrm{p}} = (\boldsymbol{F}^{\mathrm{pT}}\boldsymbol{F}^{\mathrm{p}})^{-1}$, which is related to the elastic left Cauchy–Green tensor $\boldsymbol{b}^{\mathrm{e}}$ through

$$\boldsymbol{b}^{\mathrm{e}} = \boldsymbol{F}\boldsymbol{G}^{\mathrm{p}}\boldsymbol{F}^{\mathrm{T}} \tag{12}$$

After differentiating Equation (12) with respect to time and accounting for the relation $\boldsymbol{l} = \dot{\boldsymbol{F}}\boldsymbol{F}^{-1}$, Equation (10) is expressed as

$$\dot{\boldsymbol{G}}^{\mathrm{p}} = -2\dot{\gamma}(\boldsymbol{F}^{-1}\boldsymbol{m}_\tau\boldsymbol{F})\boldsymbol{G}^{\mathrm{p}} \tag{13}$$

If associated plasticity is considered, as it is the case in the examples, it is defined by the choice

$$\boldsymbol{m}_\tau = \frac{\partial f}{\partial \boldsymbol{\tau}} \quad \text{and} \quad \boldsymbol{m}_{\mathbf{q}} = \frac{\partial f}{\partial \mathbf{q}} \tag{14}$$

2.2. Practical implementation of hyperelastoplasticity

Particle displacements $\boldsymbol{u}$ are computed with the incremental-iterative strategy commonly used in non-linear solid mechanics [10]. At every iteration within the time-step $[{}^{n}t, {}^{n+1}t]$, a displacement increment ${}^{n+1}\Delta\boldsymbol{u}$ is computed, and the hyperelastic–plastic model is then integrated with the following steps:

1. Update the spatial co-ordinates

$$
{}^{n+1}\boldsymbol{x} = {}^{n}\boldsymbol{x} + {}^{n+1}\Delta\boldsymbol{u} \tag{15}
$$

2. Compute the incremental deformation gradient

$$
{}^{n+1}\boldsymbol{f} = \frac{\partial\, {}^{n+1}\boldsymbol{x}}{\partial\, {}^{n}\boldsymbol{x}} = \boldsymbol{I} + \frac{\partial\, {}^{n+1}\Delta\boldsymbol{u}}{\partial\, {}^{n}\boldsymbol{x}} \tag{16}
$$

3. Elastic predictor. Assume that the current increment is purely elastic and define the elastic trial state as

$$
{}^{n+1}\boldsymbol{b}^{\mathrm{e}}_{\mathrm{trial}} = {}^{n+1}\boldsymbol{f}\, {}^{n}\boldsymbol{b}^{\mathrm{e}}\, {}^{n+1}\boldsymbol{f}^{\mathrm{T}} \tag{17}
$$

$$
{}^{n+1}\boldsymbol{\alpha}_{\mathrm{trial}} = {}^{n}\boldsymbol{\alpha} \tag{18}
$$

Equation (17) is simply a push-forward of the elastic left Cauchy–Green tensor at time ${}^{n}t$. This expression is obtained directly from the definition of $\boldsymbol{b}^{\mathrm{e}}$, see Equation (4), and the relation between deformation gradients, ${}^{n+1}\boldsymbol{F} = {}^{n+1}\boldsymbol{f}\, {}^{n}\boldsymbol{F}$.

4. Plastic corrector. Given the elastic trial, the constitutive Equations (9), (10) and (11) are iteratively solved (for simple yield surfaces, no iterations are needed). Corrected values ${}^{n+1}\boldsymbol{b}^{\mathrm{e}}$ and ${}^{n+1}\boldsymbol{\alpha}$ are obtained.

5. Computation of stresses and stress-like internal variables. Once the plastic corrector, step 4, has converged, Kirchhoff stresses ${}^{n+1}\boldsymbol{\tau}$ and internal variables ${}^{n+1}\boldsymbol{q}$ are computed from Equation (5):

$$
{}^{n+1}\boldsymbol{\tau} = 2\frac{\mathrm{d}W^{\mathrm{e}}}{\mathrm{d}\boldsymbol{b}^{\mathrm{e}}}({}^{n+1}\boldsymbol{b}^{\mathrm{e}})\, {}^{n+1}\boldsymbol{b}^{\mathrm{e}} \quad \text{and} \quad {}^{n+1}\boldsymbol{q} = -\frac{\mathrm{d}W^{\mathrm{p}}}{\mathrm{d}\boldsymbol{\alpha}}({}^{n+1}\boldsymbol{\alpha}) \tag{19}
$$

The Cauchy stresses are computed by means of Equation (7), namely

$$
{}^{n+1}\boldsymbol{\sigma} = \frac{{}^{n+1}\boldsymbol{\tau}}{\det({}^{n+1}\boldsymbol{F})} \tag{20}
$$

after the deformation gradient ${}^{n+1}\boldsymbol{F}$ is computed. This is usually done by direct differentiation of ${}^{n+1}\boldsymbol{x}$ with respect to $\boldsymbol{X}$. Note, however, that numerical integration of Equation (8) is also possible, because it only introduces time-integration errors of the order of those done in the plastic correction.

Remark 2. Steps 2, 3 and 4 are unnecessary in the case of hyperelasticity (i.e., no plastic strains). The deformation gradient ${}^{n+1}\boldsymbol{F}$ can be computed directly from Equation (15) as ${}^{n+1}\boldsymbol{F} = \partial\, {}^{n+1}\boldsymbol{x}/\partial\boldsymbol{X}$. After that, stresses are obtained from Equations (4) and (5)$_1$.

Remark 3. If hyperelasticity is combined with remeshing (at, say, time ${}^{n}t$), the mapping information between ${}^{n}\boldsymbol{x}$ and $\boldsymbol{X}$ is lost, so Remark 2 does not apply. The incremental approach

just discussed is again needed (without the plastic correction, step 4). Once $^{n}b^{e}$ is projected from the old mesh to the new mesh, the elastic tensor is computed at time ^{n+m}t, $m \geqslant 1$ simply as $^{n+m}b^{e} = {}^{n+m}f{}^{n}b^{e\,n+m}f^{T}$, where

$$^{n+m}f = \frac{\partial^{\,n+m}x}{\partial^{\,n}x} \tag{21}$$

3. BASIC ALE KINEMATICS

The key ingredient of the ALE formulation is the referential configuration R_{χ}, with grid (or reference) points χ used as independent variables to describe body motion. This referential configuration R_{χ} is mapped into the material and spatial configurations by Ψ and Φ respectively, see Figure 1:

$$X = \Psi(\chi, t) \tag{22}$$

and

$$x = \Phi(\chi, t) \tag{23}$$

with the corresponding deformation gradients

$$F_{\Psi}(\chi, t) = \frac{\partial \Psi}{\partial \chi}(\chi, t) \quad \text{and} \quad F_{\Phi}(\chi, t) = \frac{\partial \Phi}{\partial \chi}(\chi, t) \tag{24}$$

The three mappings φ, Φ and Ψ are related by

$$\varphi = \Phi \circ \Psi^{-1} \tag{25}$$

Direct application of the chain rule to Equation (25) leads to the relation between the three deformation gradients defined in Equations (2) and (24):

$$F = F_{\Phi} F_{\Psi}^{-1} \tag{26}$$
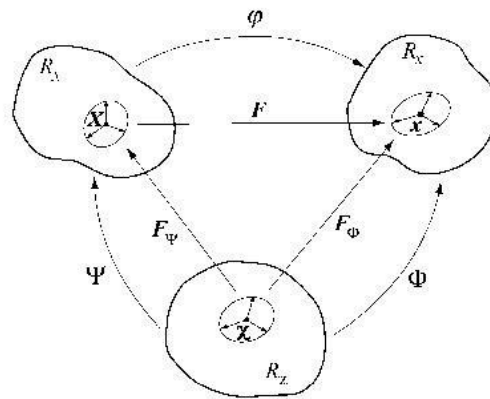
Figure 1. Domains, mappings and deformation gradients in the ALE description.

In an ALE setting, two displacement fields can be defined on the referential configuration: the material displacement u_Ψ

$$u_\Psi(\chi,t) = X(\chi,t) - \chi \tag{27}$$

and the spatial displacement u_Φ

$$u_\Phi(\chi,t) = x(\chi,t) - \chi \tag{28}$$

These two displacement fields describe how the material particles and the spatial points, respectively, move with respect to the grid points.

Remark 4. In general, the three displacement fields (u, u_Ψ and u_Φ) are different. Note that *material* displacements are defined according to Equation (27), so the notation *particle* displacements is used to refer to the 'real' (i.e., physically meaningful) displacements, Equation (1).

The fundamental ALE relationship between material time derivatives and referential time derivatives is [7]

$$\left.\frac{\partial(\cdot)}{\partial t}\right|_X = \left.\frac{\partial(\cdot)}{\partial t}\right|_\chi + c\nabla_x(\cdot) \tag{29}$$

where the so-called convective velocity c (i.e., the difference between particle velocity v and mesh velocity $\hat{v} = \partial x/\partial t|_\chi$) can be computed from the corresponding displacement increments:

$$c = v - \hat{v} = [^{n+1}\Delta u(\chi) - {}^{n+1}\Delta u_\Phi(\chi)]/\Delta t \tag{30}$$

Note that the fundamental unknowns are the increment of particle displacements $^{n+1}\Delta u(\chi)$ and the increment of spatial (or mesh) displacements $^{n+1}\Delta u_\Phi(\chi)$.

4. $F^e F^p$ FINITE-STRAIN PLASTICITY IN AN ALE SETTING

Going through the algorithm of Section 2.2 reveals that time derivatives only appear in three equations, namely Equations (10), (11) and (8). Using the fundamental ALE relationship, these equations can be rewritten into their ALE format,

$$\left.\frac{\partial b^e}{\partial t}\right|_\chi + c\nabla_x b^e = lb^e + b^e l^T - 2\dot{\gamma} m_\tau(\tau,q)b^e \tag{31}$$

$$\left.\frac{\partial \alpha}{\partial t}\right|_\chi + c\nabla_x \alpha = \dot{\gamma} m_q(\tau,q) \tag{32}$$

$$\left.\frac{\partial |F|}{\partial t}\right|_\chi + c\nabla_x |F| = |F|\nabla_x \cdot v \tag{33}$$

simply by replacing the material time derivative with a referential time derivative and a convective term. Equations (31)–(33) are in the so-called 'quasi-Eulerian' format commonly encountered in ALE fluid dynamics and ALE hypoelastoplasticity [15].

4.1. Influence of the ALE setting on the implementation of hyperelastoplasticity

The algorithm of Section 2.2 can be adapted in a simple manner to account for the ALE setting. The resulting algorithm is as follows:

1. Update the spatial co-ordinates (*unaffected by ALE setting*)

$$^{n+1}x = {}^{n}x + {}^{n+1}\Delta u$$

2. Compute the incremental deformation gradient (*unaffected by ALE setting*)

$$^{n+1}f = \frac{\partial\, ^{n+1}x}{\partial\, ^{n}x} = I + \frac{\partial\, ^{n+1}\Delta u}{\partial\, ^{n}x}$$

3. Elastic predictor (*unaffected by ALE setting*). Assume that the current increment is purely elastic and define the elastic trial state as

$$^{n+1}b^{e}_{trial} = {}^{n+1}f\, ^{n}b^{e}\, ^{n+1}f^{T}$$

$$^{n+1}\alpha_{trial} = {}^{n}\alpha$$

4. Plastic corrector. Given the elastic trial, constitutive equations (9), (31) and (32) are solved. The convective terms in Equations (31) and (32) are accounted for by the numerical time-integration algorithm (*influence of ALE setting*). Corrected values $^{n+1}b^{e}$ and $^{n+1}\alpha$ are obtained.

5. Computation of stresses and stress-like internal variables. Once the plastic corrector, step 4, has converged, Kirchhoff stresses $^{n+1}\tau$ and internal variables ^{n+1}q are computed from Equation (5) (*unaffected by ALE setting*):

$$^{n+1}\tau = 2\frac{\mathrm{d}W^{e}}{\mathrm{d}b^{e}}(^{n+1}b^{e})^{n+1}b^{e} \quad \text{and} \quad ^{n+1}q = -\frac{\mathrm{d}W^{p}}{\mathrm{d}\alpha}(^{n+1}\alpha)$$

The Cauchy stresses are computed by means of Equation (7), namely

$$^{n+1}\sigma = \frac{^{n+1}\tau}{\det(^{n+1}F)}$$

after the deformation gradient ^{n+1}F is computed via numerical time-integration of Equation (33) (*influence of ALE setting*).

It is worth noting that only step 3 and the second part of step 5 (that is, the computation of Cauchy stresses) are affected by the change from a Lagrangian to an ALE setting.

4.2. A simplified fractional-step ALE method

If an unsplit ALE approach is chosen [16], the convective terms in the LHS and the material terms in the RHS of Equations (31)–(33), see Section 4.1, are treated simultaneously. This means that ALE remeshing and convection must be accounted for at each iteration within the time-step.

Here a fractional-step method is preferred. It is a very common strategy to treat ALE convective terms [3, 5, 6, 13, 17, 18]. Every time-step is divided into two phases: the Lagrangian phase and the convection phase. During the Lagrangian phase, convection c is neglected and

Table I. The proposed ALE approach for hyperelastoplasticity.

For every time-step $[^n t, ^{n+1} t]$:

Material phase

- Neglect convective terms
- Advance the solution in a Lagrangian fashion: compute the increment of particle displacements $^{n+1}\Delta u$ and quantities $^L b^e$, $^L \alpha$ and $\det(^L F)$ (superscript L denotes Lagrangian)

Remeshing

- Compute the increment of mesh displacements $^{n+1}\Delta u_\Phi$ by means of a remeshing algorithm that reduces element distortion and update the mesh co-ordinates
- Compute the convective velocity $c = [^{n+1}\Delta u - ^{n+1}\Delta u_\Phi]/\Delta t$

Convection phase

- Account for convective terms
- Use the Godunov-type technique to convect quantities $^L b^e$, $^L \alpha$ and $\det(^L F)$ into $^{n+1} b^e$, $^{n+1}\alpha$ and $\det(^{n+1}F)$
- Compute stresses $^{n+1}\tau$ and $^{n+1}\sigma$

the increment of particle displacements $^{n+1}\Delta u(^n X(\chi))$ is computed iteratively in the usual Lagrangian fashion, as described in Section 2.2. This increment is referred to the particles $^n X$ associated to grid points χ at the beginning of the time-step, $^n X = X(\chi, ^n t)$.

After that, an ALE remeshing algorithm is employed to compute the increment of mesh displacements $^{n+1}\Delta u_\Phi(\chi)$, and the spatial co-ordinates of grid points are updated according to

$$^{n+1}x(\chi) = ^n x(\chi) + ^{n+1}\Delta u_\Phi(\chi) \qquad (34)$$

The relative motion between the material and the mesh is represented by the convective velocity c, see Equation (30).

During the convection phase, the convective terms which were neglected during the Lagrangian phase are taken into account. A Godunov-like technique [19, 6] is used to transport quantities b^e, α and $|F|$ from the old mesh to the new mesh, see Remark 5.

The proposed ALE approach for hyperelastoplasticity is summarized in Table I. Note that ALE remeshing and the convection phase are only performed once per time-step, after equilibrium is achieved in the Lagrangian phase. Numerical experimentation shows that the spurious residual forces associated to convection are small and do not affect the quality of the solution, see Section 5 and References [6, 17]. On the other hand, since explicit algorithms are used for both convection, see Equation (35), and ALE remeshing, the computational overhead of an ALE computation with respect to a Lagrangian computation is not significant.

Remark 5. The Godunov-like technique based on Godunov's method for conservation laws. It assumes piecewise constant fields, so each finite element is subdivided into various subelements, each corresponding to the influence domain of a Gauss point. Eight-noded quadrilaterals with 2×2 Gauss points are used in the numerical examples of Section 5, so each element is subdivided into four subelements. For every subelement, the scalar quantity □

(i.e., a component of b^e, an internal variable α or $|F|$) is explicitly updated according to

$$^{n+1}\square = {}^{\text{L}}\square - \frac{\Delta t}{A} \sum_{\Gamma=1}^{N_\Gamma} f_\Gamma(\square_\Gamma^{\text{c}} - \square)[1 - \text{sign}(f_\Gamma)] \tag{35}$$

where A is the area of the subelement, N_Γ is the number of edges per subelement, $\square_\Gamma^{\text{c}}$ is the value of $\square$ in the contiguous subelement across edge Γ, and f_Γ is the flux of convective velocity across edge Γ, $f_\Gamma = \int_\Gamma(c \cdot n)\mathrm{d}\Gamma$.

Remark 6. In the proposed ALE approach, the time-integration of the elastic response is not exact. Consider, for simplicity, the case of hyperelasticity, where Equations (32), (33) and the last term of Equation (31) are dropped. During the convection phase (needed to transport b^e), truncation errors are introduced. It must be noted, however, that these numerical errors can be controlled by the time-step Δt and the mesh size. They are completely unrelated with the drawbacks of hypoelastic models (i.e., elastic dissipation in a closed path). From the viewpoint of modelling, the proposed approach is fully hyperelastic.

Moreover, if the general case of hyperelastoplasticity is considered, the truncation errors associated to convection and to the plastic correction are of the same order, $\mathcal{O}(\Delta t)$: both the Godunov-like technique and the backward Euler algorithm commonly employed for the return mapping [8] are of order 1.

4.3. Comparing the proposed approach to other approaches for ALE hyperelastoplasticity

The proposed ALE approach for hyperelastoplasticity separates in a natural way the material (i.e., constitutive) and the convective effects. In fact, a similar approach can be used for ALE hypoelastoplasticity [5, 6]. The main differences are (1) the constitutive model for the Lagrangian phase (hyper/hypo) and (2) the quantities to transport in the convection phase.

It is worth noting, however, that this approach is in sharp contrast with other ALE formulations for hyperelastoplasticity reported in the literature. In References [12, 13], the fundamental unknowns are the increment of material displacements $^{n+1}\Delta u_\Psi$ (rather than the increment of particle displacements $^{n+1}\Delta u$) and the increment of spatial displacements $^{n+1}\Delta u_\Phi$. Material and spatial co-ordinates, X and x, are then updated according to $^{n+1}X(\chi) = {}^{n}X(\chi) + {}^{n+1}\Delta u_\Psi(\chi)$ and Equation (34).

After that, the deformation gradients $^{n+1}F_\Psi$ and $^{n+1}F_\Phi$ can be computed, see Equations (22) and (23), and used to compute the total deformation gradient ^{n+1}F with Equation (26). The main advantage of this approach is that it leads to an ALE formulation with no convective terms in the particular case of hyperelasticity. The spatial and material configurations, R_x and R_X, are linked via the referential configuration R_χ, and this allows the computation of F, which is the basic ingredient to compute the stresses, Equations (3)–(5).

However, there is also a major drawback: it is essential to avoid element distortion or entanglement in *two* mappings: Ψ and Φ. If not, gradients F_Ψ and/or F_Φ cannot be properly computed. This is rather cumbersome and limits the potential of the ALE approach as an *r*-adaptive technique. In the approach proposed here, on the contrary, the mapping Ψ is not tracked at all, so the only concern when relocating the nodes in the ALE remeshing algorithm is the quality of the spatial mesh (i.e., the mapping of the finite element mesh in the referential domain R_χ into the spatial domain R_x).

Moreover, convective terms appear anyway in the general case of hyperelastoplasticity. In Reference [13], Equation (13) is rewritten in an ALE setting as

$$\frac{\partial \boldsymbol{G}^{\mathrm{p}}}{\partial t}|_{\boldsymbol{\chi}} - \boldsymbol{\nabla}_{\boldsymbol{\chi}} \boldsymbol{G}^{\mathrm{p}} \cdot \boldsymbol{F}_{\boldsymbol{\Psi}}^{-1} \frac{\partial \boldsymbol{X}}{\partial t}|_{\boldsymbol{\chi}} = -2\dot{\gamma}(\boldsymbol{F}^{-1} \boldsymbol{m}_{\tau} \boldsymbol{F}) \boldsymbol{G}^{\mathrm{p}} \tag{36}$$

Note that the material time derivative in the LHS of Equation (13) is transformed, in Equation (36), into a referential time derivative and a convective term which accounts for the relative motion between material particles $\boldsymbol{X}$ and grid points $\boldsymbol{\chi}$. A similar result is obtained for Equation (11).

In this context, the need of convecting $\boldsymbol{b}^{\mathrm{e}}$ for ALE hyperelasticity is not a significant drawback of the proposed approach, see also Remark 6.

5. NUMERICAL EXAMPLES

The proposed ALE approach is illustrated and validated here by means of three representative numerical examples: a necking test, a coining test and a powder compaction test. Eight-noded quadrilateral elements with 2×2 Gauss-points are employed for all the computations.

5.1. Necking test

The necking problem is a well-known benchmark test in large-strain solid mechanics [20, 6, 21, 22]. A cylindrical bar with circular cross-section, with a radius of 6.413 mm and 53.334 mm length, is subjected to uniaxial extension. A slight geometric imperfection (1 per cent reduction in radius), see Figure 2, induces necking in the central part of the bar. An axisymmetric analysis is carried out with the mesh of 5×10 finite elements shown in Figure 2.

Two hyperelastic–plastic models have been used: the classical von Mises model [8, 11] and a Tresca-type model [21], which depends on a yield shape parameter. This parameter controls the smoothing of the yield surface corners and ranges from 1 (von Mises yield surface) to ∞ (Tresca yield surface). The two models are isochoric and exhibit hardening. In consequence, the quantities to transport in the convection phase are $\boldsymbol{b}^{\mathrm{e}}$ and $\boldsymbol{\alpha}$, which contains one internal plastic variable. The material parameters for both models are summarized in Table II, see References [20, 23] for further details.

For comparative purposes, both Lagrangian and ALE analyses have been performed. A very simple ALE remeshing strategy is used [6]: the outer region BDEG of the mesh is Lagrangian, and equal height of elements is prescribed in the central region ABGH.

The results with the von Mises model are discussed first. Figure 3 depicts the deformed shapes up to an elongation d of 8 mm for half the bar. As expected, the elements in the neck zone become very distorted with the Lagrangian description, see Figure 3(a)–3(c). The distortion is highly reduced with the ALE description, see Figure 3(d)–3(f). In the proposed ALE approach, the quality of these spatial meshes is the only concern of the ALE remeshing strategy. There is no need to ensure the quality of the material meshes [12, 13].

A more quantitative comparison is offered in Figure 4, which shows the evolution of the vertical reaction and dimensionless radius (ratio of current radius to initial radius) with elongation. Very similar results are obtained up to an elongation of 6.5–7 mm. If pulling
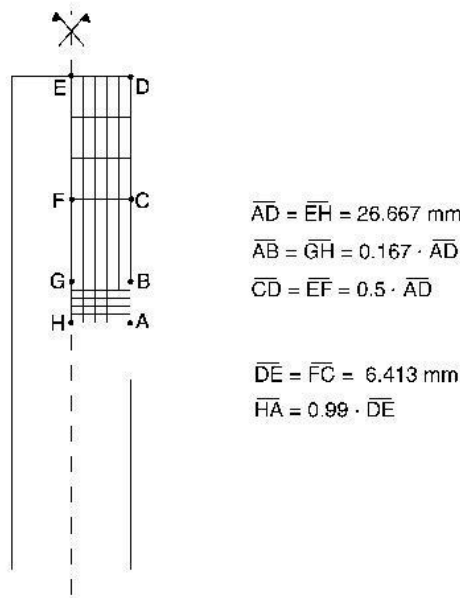
$$\overline{AD} = \overline{EH} = 26.667 \text{ mm}$$

$$\overline{AB} = \overline{GH} = 0.167 \cdot \overline{AD}$$

$$\overline{CD} = \overline{EF} = 0.5 \cdot \overline{AD}$$

$$\overline{DE} = \overline{FC} = 6.413 \text{ mm}$$

$$\overline{HA} = 0.99 \cdot \overline{DE}$$

Figure 2. Necking of a cylindrical bar. Problem definition and computational mesh.

Table II. Material parameters for the necking test.

Bulk modulus	164.206 GPa
Shear modulus	80.1938 GPa
Initial flow stress	0.45 GPa
Residual flow stress	0.715 GPa
Linear hardening coefficient	0.12924 GPa
Saturation exponent	16.93
Yield shape exponent (Tresca-type model)	20

proceeds, however, discrepancies arise between the Lagrangian and ALE solutions. With only one row of (very distorted) elements in the necking zone, the Lagrangian simulation on the coarse mesh does not fully capture the plastification process, and this results in less necking. The ALE response is in much better agreement with a reference Lagrangian solution with a very fine mesh (not shown in the figure).

A final, qualitative assessment of the two simulations can be made by looking at the distribution of the von Mises stress. According to some empirical and semianalytical studies [24] this field is constant in the neck zone, along the $z = 0$ plane of symmetry. Plate 1 shows the distribution of the von Mises stress after an elongation of 7 mm. It can be seen that the Lagrangian analysis, Plate 1(a), does not provide a constant value along $z = 0$, while the ALE analysis does, Plate 1(b). The results reported in Reference [6] for the hypoelastic–plastic von Mises model are shown in Plate 1(c) and 1(d). Since elastic strains are small compared to elastic strains for this test, the hyperelastic and hypoelastic approaches yield very similar results.

The same test is performed with the Tresca-type model. Figure 5 shows the deformed shapes as elongation proceeds. The highly distorted Lagrangian meshes show the different
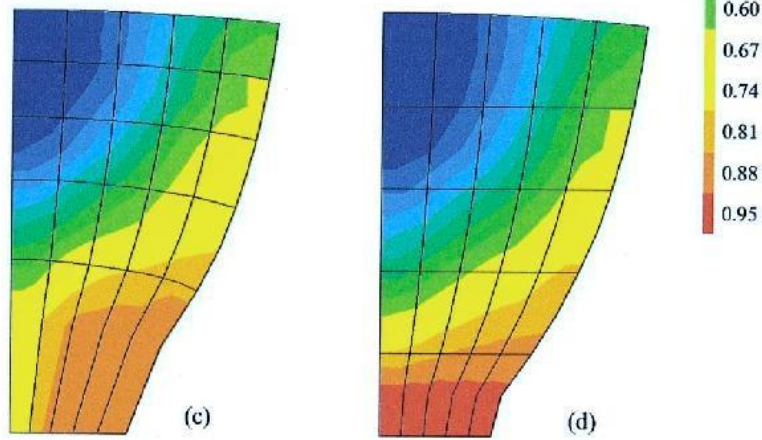
Hyperelastic model
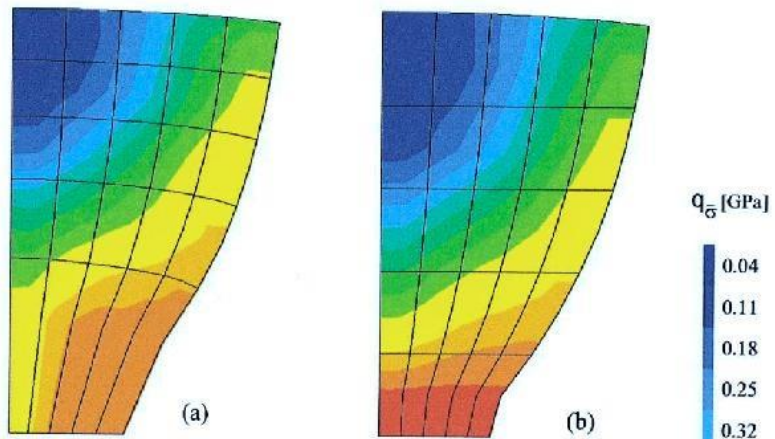
Hypoelastic model

Plate 1. Necking test with the von Mises model. Distribution of the von Mises stress in the necking zone. Hyperelastic–plastic model: (a) Lagrangian formulation; (b) ALE formulation. Hypoelastic–plastic model (after Reference [6]): (c) Lagrangian formulation; (d) ALE formulation.
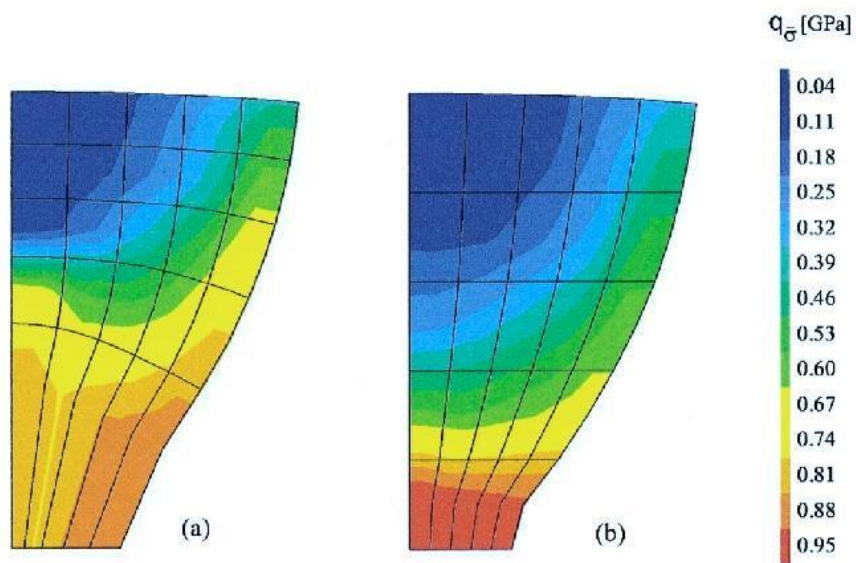
Plate 2. Necking test with the Tresca-type model. Distribution of the von Mises stress in the necking zone: (a) Lagrangian formulation; (b) ALE formulation.
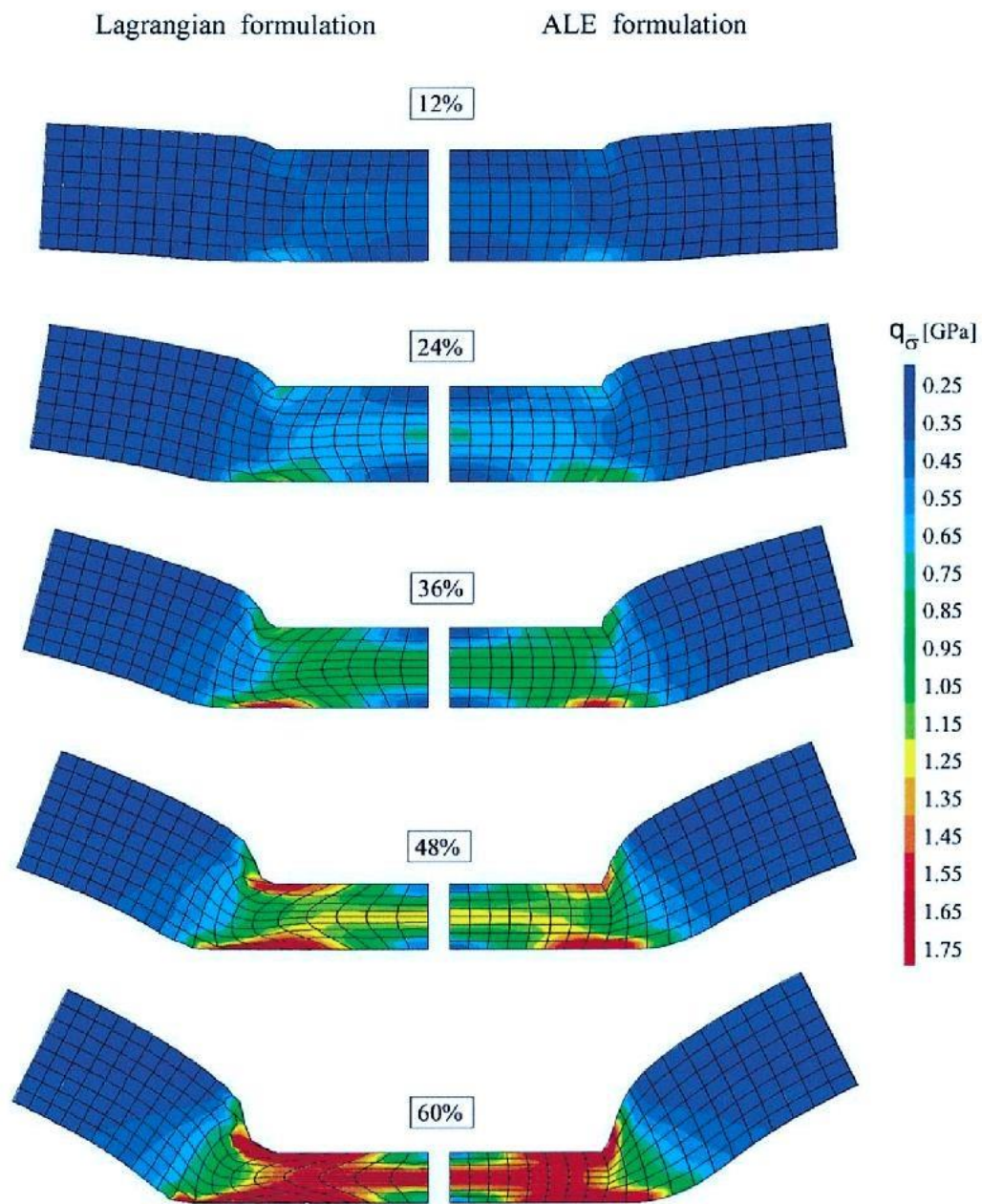
Lagrangian formulation   ALE formulation

12%

24%

q_σ [GPa]

0.25
0.35
0.45
0.55
0.65
0.75
0.85
0.95
1.05
1.15
1.25
1.35
1.45
1.55
1.65
1.75

36%

48%

60%

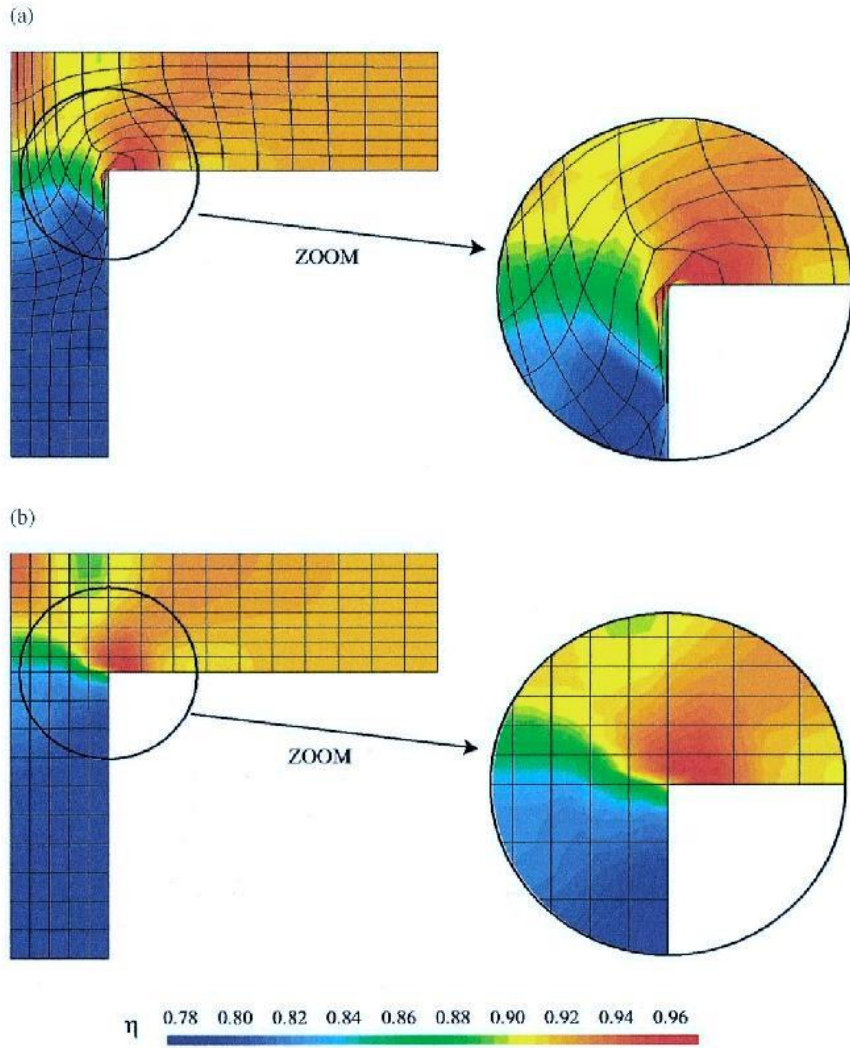Plate 3. Coining test with the von Mises model. Mesh configurations and distribution of the von Mises stress for different height reductions. Lagrangian and ALE formulations.

(a)

ZOOM

(b)

ZOOM

η 0.78   0.80   0.82   0.84   0.86   0.88   0.90   0.92   0.94   0.96

Plate 4. Top punch compaction of the flanged component. Final relative density distribution after a punch displacement of 6.06 mm: (a) Lagrangian formulation; and (b) ALE formulation.
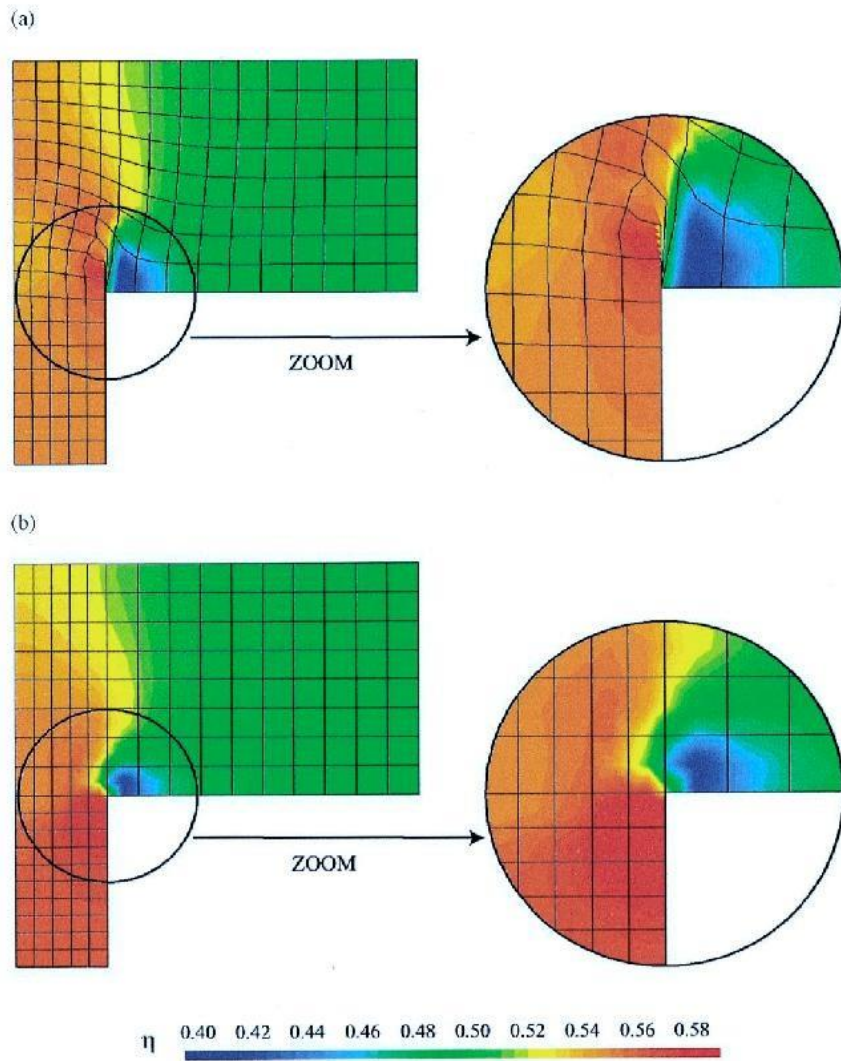
(a)

ZOOM

(b)

ZOOM

η   0.40   0.42   0.44   0.46   0.48   0.50   0.52   0.54   0.56   0.58

Plate 5. Bottom punch compaction of the flanged component. Final relative density distribution after a punch displacement of 5.10 mm: (a) Lagrangian formulation; and (b) ALE formulation.
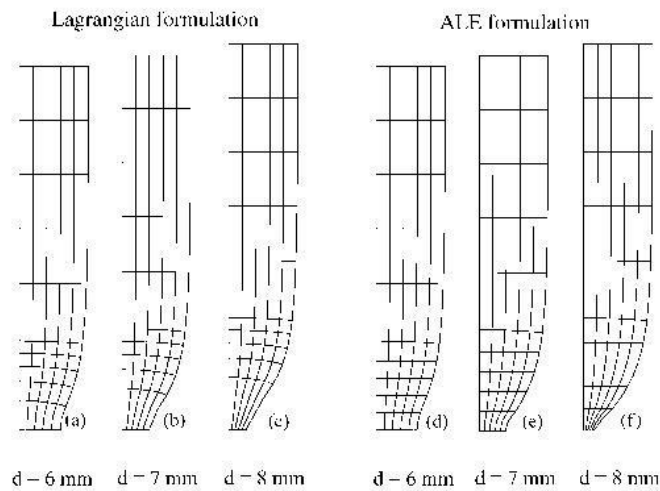
Figure 3. Necking test with the von Mises model. Mesh configurations for different top displacements d: (a)–(c) Lagrangian formulation; and (d)–(f) ALE formulation.
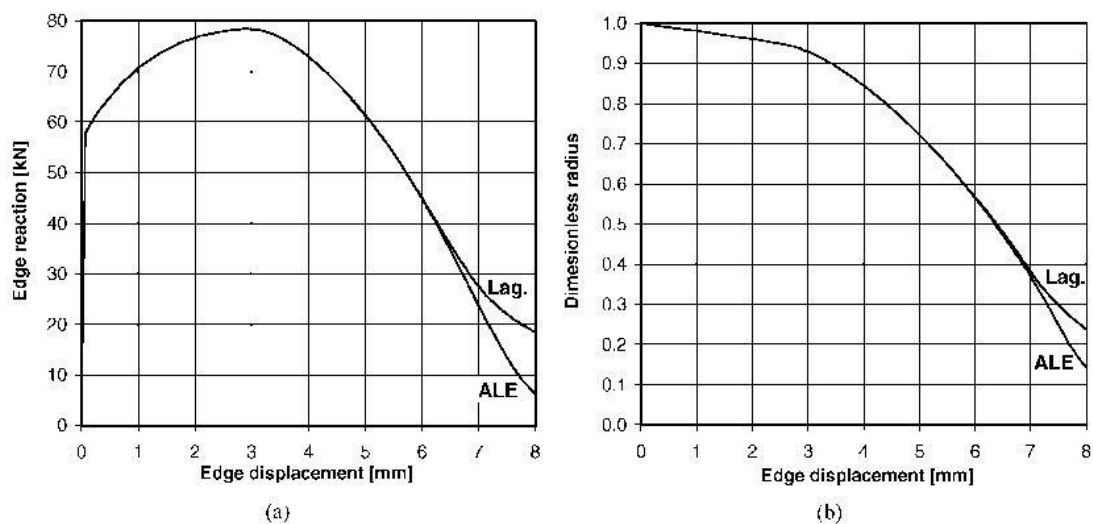

Figure 4. Necking test with the von Mises model. Lagrangian and ALE formulations. Global response: (a) vertical edge reaction; and (b) dimensionless radius in the necking zone versus vertical edge displacement.

failure pattern with respect to the von Mises model, compare Figures 3(a)–3(c) and 5(a)–5(c). The ALE meshes, however, are very similar, compare Figures 3(d)–3(f) and 5(d)–5(f), because the same ALE remeshing strategy is used. Owing to the ALE description, the quality of the spatial mesh can be ensured independently of the material deformation.
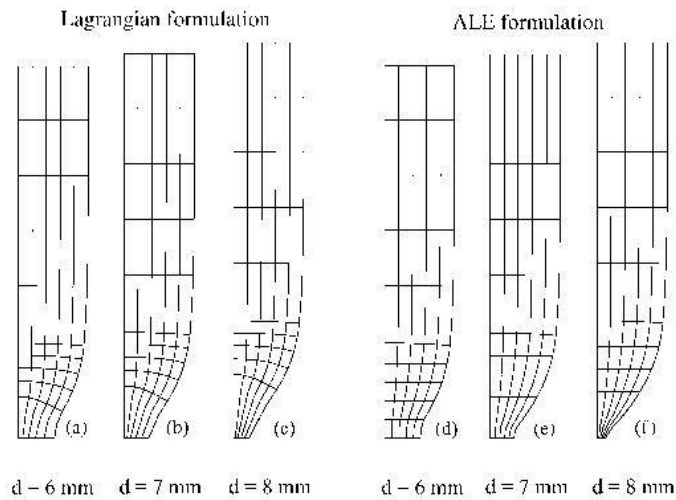
Figure 5. Necking test with the Tresca-type model. Mesh configurations for different top displacements, d: (a)–(c) Lagrangian formulation; and (d)–(f) ALE formulation.
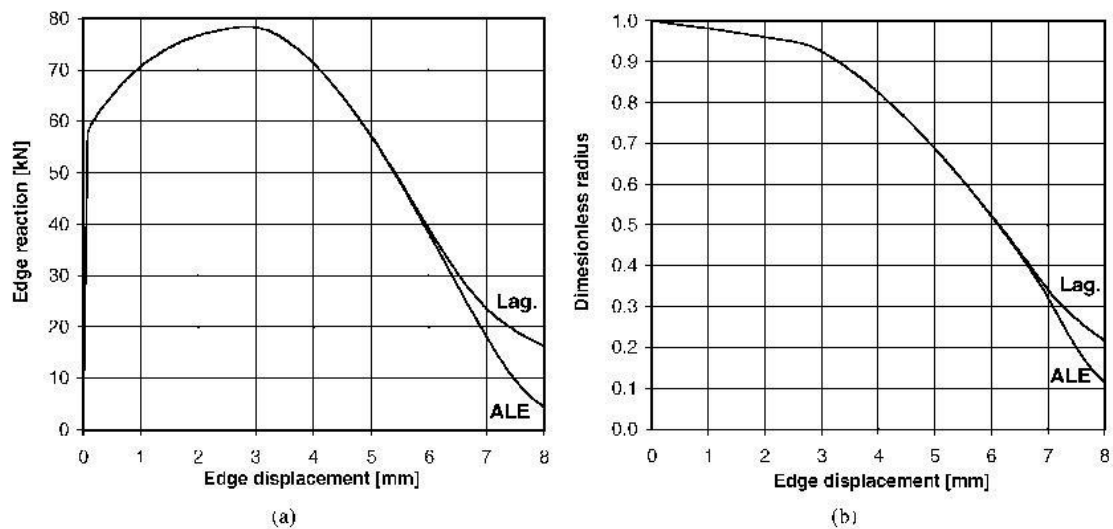

Figure 6. Necking test with the Tresca-type model. Lagrangian and ALE formulations. Global response: (a) vertical edge reaction; and (b) dimensionless radius in the necking zone versus vertical edge displacement.

Regarding the structural response and the von Mises stress distribution, results with the Tresca material are qualitatively very similar to those with the von Mises model. Figure 6 shows that the global behaviour of the piece is captured correctly with the Lagrangian formulation only up to an elongation of 6.5–7 mm; Plate 2 shows that only the ALE formulation correctly captures the constant stress distribution in the neck zone.
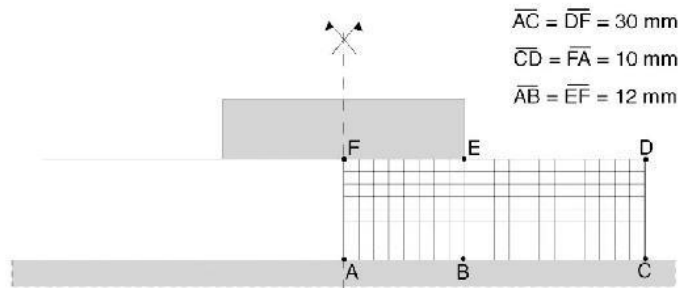
Figure 7. Coining test. Problem definition and computational mesh.

5.2. Coining test

As a second example, a coining process is simulated [6]. A metallic disk, with a radius of 30 mm and a height of 10 mm, is deformed by a punch 12 mm in radius, see Figure 7. The von Mises hyperelastic–plastic model is employed, with elastic modulus $E = 200$ GPa, Poisson's coefficient $v = 0.3$, yield stress $\sigma_y = 250$ MPa and plastic modulus $E_p = 1$ GPa. Both the punch and the die are rigid. Perfect friction (stick) conditions are assumed in the punch–disk and disk–die interfaces. An axisymmetric analysis is performed to model a 60 per cent height reduction with a mesh of 20×8 finite elements.

Again, both a Lagrangian and an ALE analysis have been performed. The evolution of the deformed shape and the von Mises stress field is depicted in Plate 3. Owing to the stick conditions in the two interfaces, the material in the central part of the disk flows outward. This leads to a highly distorted Lagrangian mesh, especially under the punch corner and in the contact with the die. Remarkably, the convergence of the Lagrangian analysis is not disturbed by the mesh distortion, thanks to the use of consistent tangent matrices and a 2×2 Gauss-point quadrature, with negative Jacobians less likely than with a 3×3 quadrature.

The mesh distortion is greatly reduced in the ALE analysis. The following remeshing strategy is used: (1) line $\overline{AB}$ is Eulerian, lines $\overline{CD}$ and $\overline{EF}$ are Lagrangian and equal length of elements is prescribed in lines $\overline{BC}$, $\overline{CF}$ and $\overline{DA}$; (2) parabolic profiles of horizontal mesh displacements are prescribed in region ABEF and (3) mesh displacements in region BCDE are interpolated from the contour values.

As expected, the mesh distortion clearly affects the numerical solution. In Figure 8, the Lagrangian and ALE solutions are compared in terms of the displacement of points C and D and the punch reaction (radial and vertical components shown separately). For all the outputs, the two descriptions provide very similar results up to a height reduction of 20–30 per cent, which induces a relatively small distortion in the Lagrangian mesh. Significant differences, however, are encountered for increasing height reductions and a more distorted Lagrangian mesh. The same type of behaviour is obtained with the Tresca-type model (with the same material parameters used for the von Mises analysis plus the yield shape exponent equal to 20).

5.3. Compaction test

As a last example, the powder compaction of a flanged component is analysed [25]. The axisymmetric computational domain and the structured mesh of 170 finite elements are
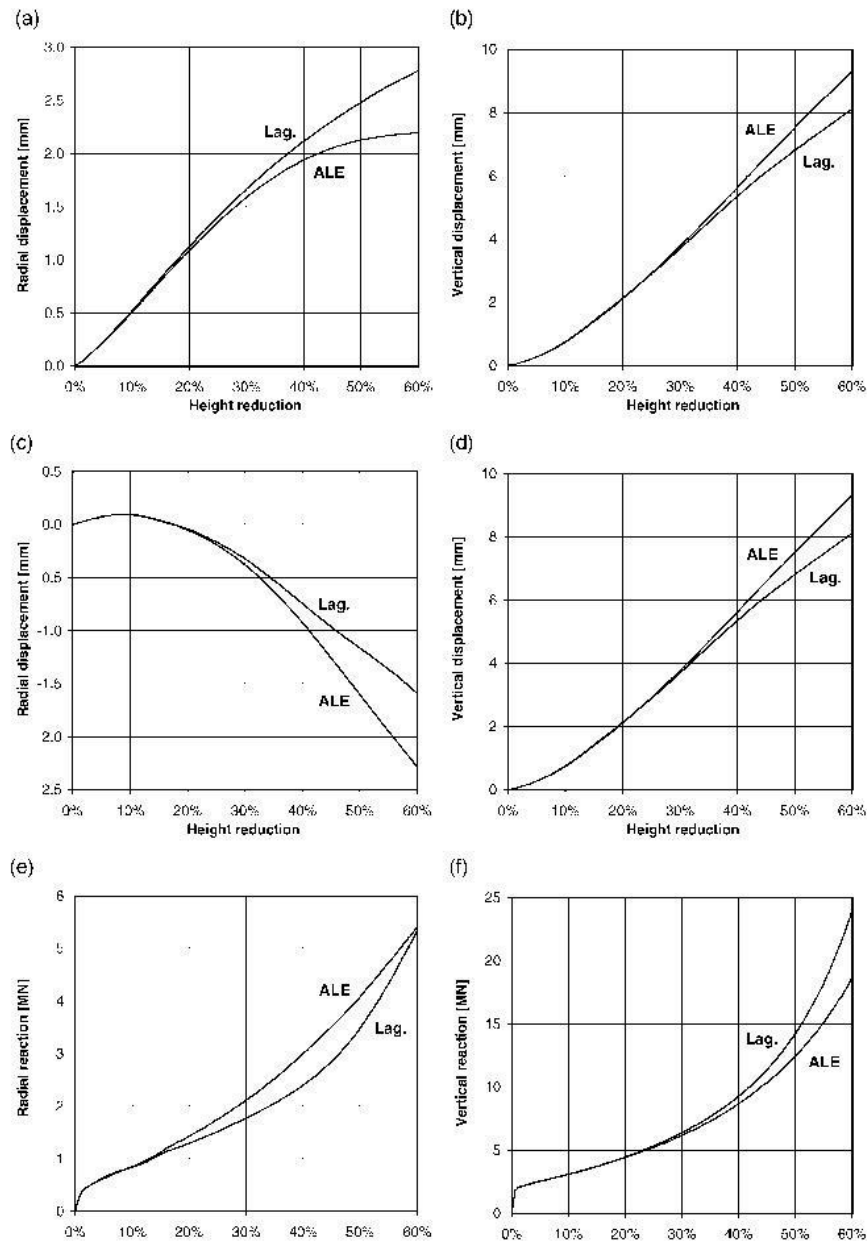
Figure 8. Coining test with the von Mises model. Lagrangian and ALE formulations. Representative results: (a), (b) point C displacements; (c), (d) point D displacements; and (e), (f) punch reactions.

depicted in Figure 9. The plastic model is non-isochoric and has no internal variables. The yield function is elliptic and depends on the density. These are usual features in plastic models for powder compaction [26]. A brief presentation of this model, together
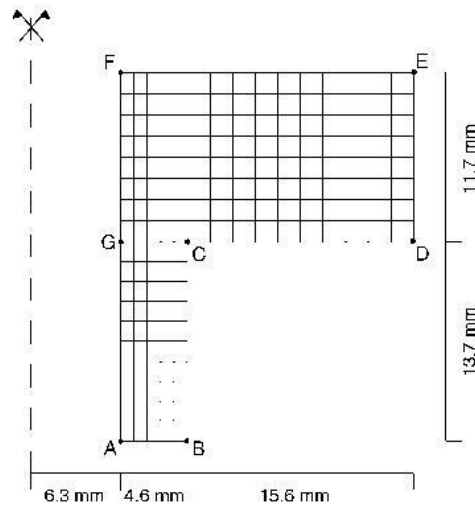
Figure 9. Flanged component. Problem definition and computational mesh, after Reference [25].

with the set of material parameters, can be found in Appendix A, see Reference [27] for further details.

Friction effects are neglected both in Reference [27] and here, because the focus of these papers are, respectively, the consistent linearization for density-dependent plastic models and the ALE kinematical description of hyperelastoplasticity. A more realistic simulation of the compaction process can be found in Reference [28], where the friction in the die wall is accounted for.

Two different processes are analysed: top punch compaction and bottom punch compaction. For comparative purposes, both Lagrangian and ALE analyses are performed. For the ALE computations, b^e and $\det(\boldsymbol{F})$ are transported during the convection phase.

Figure 10 shows a sequence of deformed meshes for different values of the top punch displacement, up to a final value of 6.06 mm. The Lagrangian meshes, Figure 10(a)–10(d), clearly shows the pattern of powder motion: as expected, the material flows to the left and to the bottom. This motion is especially important around the punch corner C. This leads to highly distorted elements in this zone, which in turn result in spurious oscillations of the relative density distribution, see Plate 4(a).

Mesh distortion can be controlled in an effective way by means of a very simple ALE remeshing strategy: (1) region ABCG remains Eulerian; (2) in region GDEF, horizontal mesh displacements are restrained and an equal height for all elements is prescribed. By doing so, the original rectangular shape of the elements is maintained throughout the whole compaction process, see Figure 10(e)–10(h). As a consequence, a smoother field of relative densities is obtained, with no spurious oscillations, see Plate 4(b).

A similar situation is encountered with the bottom compaction process. Owing to the geometry of the piece, the material motion is predominantly upwards, as the Lagrangian meshes of Figure 11(a)–11(d) show. Note the high shear distortion around the punch corner C for the final punch displacement of 5.10 mm, which concentrates in a single element. This distortion is completely eliminated with the ALE analysis. The remeshing strategy is a straightforward
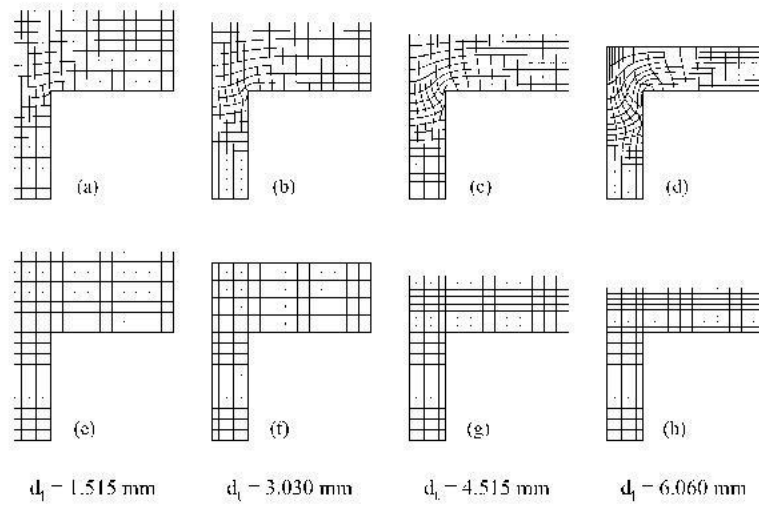
$d_t = 1.515$ mm $d_t = 3.030$ mm $d_t = 4.515$ mm $d_t = 6.060$ mm

Figure 10. Top punch compaction of the flanged component. Mesh configurations for different punch displacements d_t: (a)–(d) Lagrangian formulation; and (e)–(h) ALE formulation.

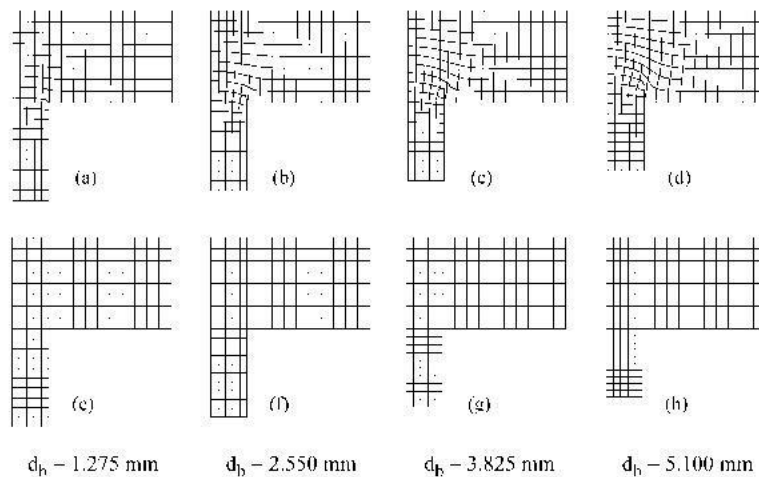$d_b = 1.275$ mm $d_b = 2.550$ mm $d_b = 3.825$ mm $d_b = 5.100$ mm

Figure 11. Bottom punch compaction of the flanged component. Mesh configurations for different punch displacements d_b: (a)–(d) Lagrangian formulation; and (e)–(h) ALE formulation.

adaptation of the one used before (i.e., region GDEF is Eulerian, and elements of equal shape are prescribed in region ABCG).

The quality of the mesh again affects the final density distribution (see Plate 5). With the Lagrangian analysis, a spurious zone of high density results near point C. With the ALE analysis, on the other hand, a smoother density field is obtained.

6. CONCLUDING REMARKS

The proposed approach allows the combination of the arbitrary Lagrangian–Eulerian kinematical description and hyperelastic–plastic models in a straightforward and effective manner. Since a fractional-step method is chosen for numerical time-marching, the material terms and the convection terms of the ALE governing equations are treated separately. As a consequence, the standard predictor–corrector techniques of finite-strain plasticity can be employed during the Lagrangian phase, and a simple Godunov-type algorithm for the convection phase.

Contrary to other approaches for ALE hyperelastoplasticity reported in the literature, the deformed configuration at the beginning of the time-step, rather than the initial configuration, provides the reference to describe the deformation. In exchange for the need of convecting the elastic strains—a marginal drawback, since plastic variables must be convected anyway—, the strategy suggested here has a major advantage: only the quality of the spatial mesh, not of the spatial and material meshes, must be ensured. This is the standard situation in ALE fluid dynamics and ALE hypoelastoplasticity, and renders a flexible r-adaptive technique.

These aspects have been illustrated by means of various numerical examples involving different hyperelastic–plastic models. The comparison of Lagrangian and ALE analyses clearly shows that it is essential to keep mesh distortion under control to ensure the quality of the numerical solution. In the ALE simulations, the distortion of the spatial mesh is controlled by means of very simple remeshing strategies, which do not have to worry about the distortion of the material mesh.

APPENDIX A

The elliptic yield function used in Section 5.3 is given by the following expression [26]:

$$f_{\text{ellip}}(\tau, \eta) = 2J_2(\tau) + a_1(\eta)\left(\frac{I_1(\tau)}{3}\right)^2 - \frac{2}{3}a_2(\eta)(\sigma_y)^2 \tag{A1}$$

with η equal to the relative density, $I_1(\tau)$ to the first invariant of τ, $J_2(\tau)$ to the second invariant of the deviatoric part of τ, and the density-dependent parameters

$$a_1(\eta) = \begin{cases} \left(\dfrac{1-\eta^2}{2+\eta^2}\right)^{n_1}, & \eta < 1 \\ 0, & \eta \geq 1 \end{cases}$$

$$a_2(\eta) = \begin{cases} \left(\dfrac{0.02\eta_0}{1-0.98\eta_0}\right)^{n_2}, & \eta \leq \eta_0 \\ \left(\dfrac{\eta - 0.98\eta_0}{1-0.98\eta_0}\right)^{n_2}, & \eta > \eta_0 \end{cases} \tag{A2}$$

The value of $a_1(\eta)$ decreases from 2^{-n_1} at $\eta = 0$ to zero for $\eta \geq 1$. Parameter $a_2(\eta)$ increases monotonically from a minimum value for $\eta \leq \eta_0$ and its value at $\eta = 1$ is one. The trace of the yield function on the meridian plane $p_\tau - q_\tau$, with $p_\tau = -I_1(\tau)/3$ and $q_\tau = \sqrt{3J_2(\tau)}$, and for different relative densities are depicted in Figure A1. The intersection with the deviatoric axis is
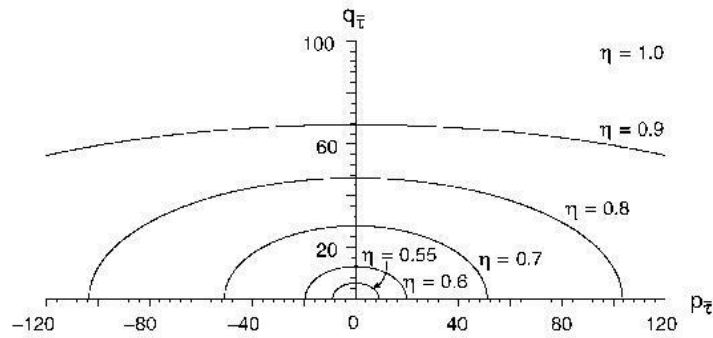
Figure A1. Traces of the elliptic yield function on the meridian plane $q_{\bar{\tau}}-p_{\bar{\tau}}$ for different relative densities, η. Material parameters from Table A1.

Table A1. Set of material parameters.

E	2000 (MPa)	v	0.37
σ_y	90 (MPa)	η_0	0.489
n_1	1	n_2	2.7

at $q_\tau = \sqrt{a_2(\eta)}\,\sigma_y$ and the intersection with the hydrostatic axis is at $p_\tau = \pm\sqrt{(2a_2(\eta)/3a_1(\eta))}\,\sigma_y$. Thus, f_{ellip} becomes the von Mises yield function for $\eta \geqslant 1$.

REFERENCES

1. Liu WK, Belytschko T, Chang H. An Arbitrary Lagrangian–Eulerian finite element method for path-dependent materials. *Computer Methods in Applied Mechanics and Engineering* 1986; **58**:227–245.
2. Benson DJ. An efficient, accurate, simple ALE method for non-linear finite element programs. *Computer Methods in Applied Mechanics and Engineering* 1986; **72**:305–350.
3. Huétink J, Vreede PT, van der Lugt J. Progress in mixed Eulerian–Lagrangian finite element simulation of forming processes. *International Journal for Numerical Methods in Engineering* 1990; **30**:1441–1457.
4. Ghosh S, Kikuchi N. An Arbitrary Lagrangian–Eulerian finite element method for large deformation analysis of elastic-viscoplastic solids. *Computer Methods in Applied Mechanics and Engineering* 1999; **86**:127–188.
5. Huerta A, Casadei F. New ALE applications in non-linear fast-transient solid dynamics. *Engineering Computations* 1994; **11**:317–345.
6. Rodríguez-Ferran A, Casadei F, Huerta A. ALE stress update for transient and quasistatic processes. *International Journal for Numerical Methods in Engineering* 1998; **43**:241–262.
7. Donea J. Arbitrary Lagrangian–Eulerian finite element methods. In *Computational Methods for Transient Analysis*, Belytschko T, Hughes TJR (eds). North-Holland: Amsterdam, 1983; 473–516.
8. Simo JC, Hughes TJR. *Computational Inelasticity*. Springer-Verlag: Berlin, 1998.
9. Bonet J, Wood RD. *Nonlinear Continuum Mechanics for Finite Element Analysis*. Cambridge University Press: Cambridge, 1997.
10. Belytschko T, Liu WK, Moran B. *Nonlinear Finite Elements for Continua and Structures*. Wiley: New York, 2000.
11. Simo JC. Numerical Analysis and Simulation of Plasticity. In *Handbook of Numerical Analysis*, Vol VI. Ciarlet PG, Lions JL (eds). Elsevier: Amsterdam, 1998; 179–499.
12. Yamada T, Kikuchi F. An arbitrary Lagrangian–Eulerian finite element method for incompressible hyperelasticity. *Computer Methods in Applied Mechanics and Engineering* 1993; **102**:149–177.
13. Armero F, Love E. An arbitrary Lagrangian–Eulerian (ALE) finite element method for finite strain elasto-plasticity. *Technical Report No. UCB/SEMM-2000/04*, Department of Civil and Environmental Engineering, University of California, Berkeley, California, January 2000.
14. Huerta A, Rodríguez-Ferran A, Díez P, Sarrate J. Adaptive finite element strategies based on error assessment. *International Journal for Numerical Methods in Engineering* 1999; **46**:1803–1818.

15. Huerta A, Liu WK. Viscous flow with large free surface motion. *Computer Methods in Applied Mechanics and Engineering* 1988; **69**:277–324.
16. Benson DJ. Computational methods in Lagrangian and Eulerian hydrocodes. *Computer Methods in Applied Mechanics and Engineering* 1992; **99**:235–394.
17. Baaijens FPT. An U-ALE formulation of 3-D unsteady viscoelastic flow. *International Journal for Numerical Methods in Engineering* 1993; **36**:1115–1143.
18. Askes H, Rodríguez-Ferran A, Huerta A. Adaptive analysis of yield line patterns in plates with the arbitrary Lagrangian–Eulerian method. *Computers and Structures* 1998; **70**:257–271.
19. Huerta A, Casadei F, Donea J. ALE stress update in transient plasticity problems. In *Proceedings of the 4th International Conference on Computational Plasticity (COMPLAS IV)*, Vol. 2, 1995; 1865–1876.
20. Simo JC. A framework for finite strain elastoplasticity based on maximum plastic dissipation and the multiplicative decomposition: Part II. Computational aspects. *Computer Methods in Applied Mechanics and Engineering* 1988; **68**:1–31.
21. Miehe C. A formulation of finite elastoplasticity based on dual co- and contra-variant eigenvector triads normalized with respect to a plastic metric. *Computer Methods in Applied Mechanics and Engineering* 1998; **159**:223–260.
22. Perić D, de Souza Neto EA. A new computational model for Tresca plasticity at finite strains with an optimal parametrization in the principal space. *Computer Methods in Applied Mechanics and Engineering* 1999; **171**:463–489.
23. Pérez-Foguet A, Armero F. On the formulation of closest-point projection algorithms in elastoplasticity. Part II: Globally convergent schemes. *International Journal for Numerical Methods in Engineering* 2002; **53**:331–374.
24. Goicolea JM. Numerical modelling in large strain plasticity with application to tube collapse analysis. *Ph.D. Thesis*, University of London, 1985.
25. Lewis RW, Khoei AR. Numerical modelling of large deformation in metal powder forming. *Computer Methods in Applied Mechanics and Engineering* 1998; **159**:291–328.
26. Oliver J, Oller S, Cante JC. A plasticity model for simulation of industrial powder compaction processes. *International Journal of Solids and Structures* 1996; **33**(20–22):3161–3178.
27. Pérez-Foguet A, Rodríguez-Ferran A, Huerta A. Consistent tangent matrices for density-dependent finite plasticity models. *International Journal for Numerical and Analytical Methods in Geomechanics* 2001; **25**:1045–1076.
28. Pérez-Foguet A, Rodríguez-Ferran A, Huerta A. Application of an ALE formation for density-dependent hyperelastic–plastic models to the stimulation of powder compaction processes. In *Proceedings of the 4th International ESAFORM Conference on Material Forming*, Habraken AM (ed.), Liège, Belgium, 2001.